Heliyon 9 (2023) e13019

Contents lists available at ScienceDirect

Heliyon

journal homepage: www.cell.com/heliyon

Research article

Influence of Y^{3+} and La^{3+} ions on the structural, magnetic, electrical, and optical properties of cobalt ferrite nanoparticles

Nazia Khatun [a,*], Sajib Ahmed [a,b], Mohammad Sajjad Hossain [c], Syed Farid Uddin Farhad [a], Md Al- Mamun [d], Mohammad Saiful Alam [b], Most. Hosney Ara Begum [a], Nazmul Islam Tanvir [a], Mahmuda Hakim [e], Suravi Islam [a,**]

[a] Industrial Physics Division, BCSIR Laboratories Dhaka, Bangladesh Council of Scientific and Industrial Research (BCSIR), Dhaka 1205, Bangladesh
[b] Department of Applied Chemistry and Chemical Engineering, Noakhali Science and Technology University (NSTU), Bangladesh
[c] Institute of Mining, Mineralogy and Metallurgy, Bangladesh Council of Scientific and Industrial Research (BCSIR), Joypurhat 5900, Bangladesh
[d] Bangladesh Atomic Energy Center (BAEC), Dhaka 1000, Bangladesh
[e] Biomedical and Toxicology Research Institute (BTRI), Bangladesh Council of Scientific and Industrial Research (BCSIR), Dhaka 1205, Bangladesh

ARTICLE INFO

Keywords:
$CoY_{0.5x}La_{0.5x}Fe_{2-X}O_4$
Sol-gel auto combustion
Nanoparticle
Complex impedance
Band-gap

ABSTRACT

In the current study, nanocrystalline $CoY_{0.5x}La_{0.5x}Fe_{2-x}O_4$ (where x = 0.00, 0.02, 0.04, 0.06, 0.08, and 0.10) ferrites have been synthesized via a sol-gel auto combustion process. The synthesized powders were pressed into pellet forms and sintered at 900 °C for 4 h in the air. X-ray diffractometry (XRD) confirmed the single-phase cubic spinel structure of the synthesized samples having the mean crystallite domain sizes ranging from 122 and 54 nm. FTIR spectroscopic analyses revealed two strong bands within the range of 600 to 350 cm^{-1}, further confirming the cubic inverse spinel structure of the prepared materials. The surface morphologies and composition were investigated by Field Emission Scanning Electron Microscopy (FE-SEM) and Energy Dispersive X-ray (EDX) Spectroscopy. The magnetic hysteresis curves recorded at room temperature exhibit ferrimagnetic behavior. The highest coercivity (Hc~1276 Oe) was found at a high doping (x = 0.10) concentration of Y^{3+} and La^{3+} in cobalt ferrite. Dielectric constant increase with increased doping concentration whereas real-impedance and dielectric loss decrease with increased in doping concentration and applied frequency. The band gap energy increased from 1.48 to 1.53 eV with increasing Y^{3+} and La^{3+}concentrations in the UV–Vis region. The elevated levels of magnetic and dielectric substances in the ferrite nanoparticles suggest that the material could be used for magnetic recording media and high-frequency devices.

1. Introduction

Spinel ferrite nanoparticles have been broadly studied for their applications in the diverse field of science and technology due to their unique properties such as structural, electrical, thermal, and magnetic properties. These properties depend on the formulation

* Corresponding author.
** Corresponding author.
E-mail addresses: naziabcsir@gmail.com (N. Khatun), suraviislambcsir@gmail.com (S. Islam).

https://doi.org/10.1016/j.heliyon.2023.e13019
Received 5 October 2022; Received in revised form 12 January 2023; Accepted 13 January 2023
Available online 24 January 2023

process, quantity, type of dopant, high mechanical strength, and good chemical stability of the ferrites [1–6]. The general formula of spinel ferrites is AB_2O_4, where A represents divalent metal cations and B represents trivalent metal cations. On the other hand, tetrahedral and octahedral cation sites in a crystal are filled respectively by A sites and B sites in a cubic close packing with oxygen. Among the spinel ferrites, cobalt ferrite has obtained tremendous attention for its unique magnetic, catalytic, chemical stability, electric, and medical properties [7], which have been broadly employed for different technical applications in catalysis, medical diagnostics, high-frequency and magneto-recording devices, information storage systems, sensors, and therapy [8,9]. Due to their low cost and outstanding performance for high-frequency applications, cobalt ferrites are one of the most suitable magnetic materials. Cobalt ferrites may be used in fabricating high-density magnetic recording media for their characteristics, including their strong coercivity, adequate saturation magnetization, mechanical toughness, and chemical stability [10,11].

The $CoFe_2O_4$ has a face-centered cubic (FCC) structure with a large unit cell and lies in the centrosymmetric Fd3m (227) space group. Spinel ferrites are classified into three types based on their cation distribution: normal, inverse, and intermediate spinel structure. In a normal spinel $CoFe_2O_4$ structure, Co^{2+} occupies the tetrahedral (A) sites, and Fe^{3+} occupies the octahedral (B) sites. In the case of inverse spinel, Co^{2+} ions remain occupied in the octahedral sites, and Fe^{3+} ions remain uniformly allotted in tetrahedral and octahedral sites [12]. Replacing rare-earth (RE) ions with spinel nano-ferrites has flourished as a hopeful trick in developing their magnetic, dielectric, and electric properties, which depend on their material properties like synthesis method, cation distributions, and grain size [13,14]. Moreover, it plays a vital role in tailoring the physicochemical properties for many promising applications in magnetic recordings, high-frequency circuits, electronic devices, sensors, transformer cores, and telecommunications [15,16]. Besides, La^{3+} and Y^{3+} doped nano spinel ferrites have desired features used in multilayer chip inductors (MLCI), primarily employed in cellular phones, laptop computers, and video cameras with other applications [17]. Nano grain size is required for high-density recording media science it will reduce media noise for light scattering at grain boundaries. Well-crystallized nano cobalt ferrites improve magneto-recording capability and the influence of Lanthanum replacement appears advantageous [8].

The magnetic properties of spinel ferrites obtained through stoichiometry control with doped RE elements have recently gained much attention from researchers. La^{3+} (1.06 Å) and Y^{3+} (0.95 Å) have no 4f electrons and a larger ionic radius than Fe^{+2} (0.67) and Co^{+2} (0.78), suggesting that they could be used to improve structural, dielectric, and magnetic properties. Several researchers have reported a strong revolution in the structural, dielectric, electrical, optical and magnetic properties of cobalt ferrites due to the combination of RE ions such as Ce^{3+}, Dy^{3+}, Gd^{3+}, etc. and mentioned an improvement in its electrical and magnetic properties [16, 18]. R. Indhrajothi et al. investigated Lanthanum-ion-substituted $CoFe_2O_4$ as anode material for lithium-ion battery application and noticed that the substitution of La^{3+} reduced the size of crystallites and the electrical conductivity of cobalt ferrite [19]. P. Kumar observed that DC resistivity increased, but saturation magnetization was decreased with the incorporation of La^{3+} in the cobalt ferrite [20]. For instance, when La^{+3} ions were used instead of $CoFe_2O_4$ nanoparticles, the saturation magnetization went down from 97.35 emu/gm to 75.84 emu/gm, and the optical band gap went up from 1.45 eV to 1.56 eV observed by I. K. Punithavathy [9]. K. H. Sharma et al. reported that lanthanum-doped cobalt ferrite rings could be utilized on magnetic coils and computer data cables to reduce hysteresis loss [11]. The incorporation of Y^{3+} into $CoFe_2O_4$ nanoparticles increases the optical band gap from 3.39 eV to 3.91 eV and decreases the saturation magnetization from 69 emu/g to 42 emu/g noticed by S. B. Das [21].

To prepare RE doped spinel ferrite nanoparticles methods such as sol-gel method, solid-state reaction route, the sonochemical method, the flash method, the hydrothermal method, the co-precipitation method, the micro-emulsion process, etc. [17,22,23] have all been used. Among these methods, the sol-gel auto-combustion procedure is one of the finest techniques for formulating cobalt ferrite nanomaterials because it creates unpolluted, regular, and uniform nanomaterials by controlling diverse parameters like reagent density, P^H of the medium, time of reaction, and temperature. The current study used the sol-gel auto combustion method to synthesize $CoY_{0.5}xLa_{0.5}xFe_{2-x}O_4$ nanoparticles, where metal nitrates such as cobalt nitrate, yttrium nitrate, lanthanum nitrate, and ferric nitrate were used as the source materials and citric acid was used as the burning agent. In particular, spin couplings of rare-earth 3d-4f electrons and other magnetic cations have been accused of improving the magnetic sequence and increasing the net magnetization of the spins. From the perspective of potential high-frequency applications, the present study aims to investigate the Y^{3+} and La^{3+} doped Cobalt ferrite.

The magnetic, dielectric and optical properties of Cobalt ferrites are significantly changed by the addition of Y^{3+} and La^{3+}ions. Additionally, the Y^{3+} and La^{3+} ions reach the octahedral site, thus enhancing the cobalt ferrite's inversion parameter. Only a few reports on Y^{3+} and La^{3+} doped ferrites nanoparticles have been published so far. Therefore, researchers have been devoted to investigating the properties of Y^{3+} and La^{3+}doped cobalt ferrite. In this study, the change in structural, morphological, magnetic, electrical, and optical properties of non-magnetic Y^{3+} and La^{3+} doped $CoFe_2O_4$ nanoparticles are shown and discussed in more detail below.

2. Experimental details

2.1. Materials and methods

Lanthanum and Yttrium substituted spinel Cobalt Ferrite $CoY_{0.5x}La_{0.5x}Fe_{2-x}O_4$ (x = 0.00, 0.02, 0.04, 0.06, 0.08 and 0.10) were synthesized by Sol-gel auto combustion method. Highly pure analytical grade (~99.9%, Merck, Germany) Cobalt Nitrate ($Co(NO_3)_2.6H_2O$), Yttrium Nitrate ($Y(NO_3)_3.6H_2O$), Lanthanum Nitrate ($La(NO_3)_3.6H_2O$), Ferric Nitrate ($Fe(NO_3)_3.6H_2O$, Citric acid ($C_6H_8O_7$) were used as initial materials for the synthesis of cobalt ferrite-based nanomaterials. All metal nitrates and citric acid were mixed in appropriate stoichiometric amounts and dissolved in a required amount of de-ionized (DI) water to make a homogenous solution. The molar ratio of nitrates and citric acid was kept at 1:3and separately stirred for 30 min by a magnetic stirrer at room

temperature until the solutions were completely dissolved. Citric acid has a higher complexion capability and lowers combustion temperature (200 °C −250 °C), which plays an essential role in the segregation and homogeneous distribution of metal ions. These different solutions were dropwise mixed using a burette in a common beaker followed by a continuous stirring for 1 h. Ammonia was added drop-wise to keep the solution's pH at ~7.0. The resulting pH-controlled solution was placed on top of the hot plate with a magnetic stirrer and stirred vigorously at 85 °C for 2–3 h to make the desired sol. Afterward, the sol was further heated until a viscous brown gel was formed. It was transferred to a furnace at a temperature of 200 °C for about 20 min, where the self-combustion occurred, and a fluffy loose dry ash was produced. Then, the obtained ash was grounded with a mortar pestle to prepare fine powder. 2 wt% polyvinyl alcohol (PVA) was mixed with the powder as a binder to form pellets through a hydraulic press machine where 3 ± 0.5 MPa pressures [2] was applied for 5 min. The prepared green pellets were sintered at 900 °C in a furnace for 4 h in the air. Finally, the pellets surface was polished by fine abrasive paper to better contact with sample holder of an impedance analyzer and silver paste was add to in both sides to improve electrical conductivity. Schematic diagram for the synthesis of Y^{3+} and La^{3+} doped Cobalt ferrite nanoparticles by sol-gel auto combustion process is shown in Fig. 1.

2.2. Analysis of the data

The X-ray diffractometer was employed to analyze the structural analysis and phase formation of the prepared samples (XRD; Rigaku, Smart Lab). Cu-Kα radiation (λ = 1.5406 °A) was used to analyze the XRD pattern at a scanning speed of 10.00°/min at room temperature with 40 KV at 40 mA and 0.02° step width in the 2θ range10°–80° range. Utilizing (*hkl)* values and inter-planar spacing, the cubic structure's lattice parameters were determined from XRD data by the following relation [2]:

$$a = d_{hkl}\sqrt{h^2 + k^2 + l^2} \tag{1}$$

where *d* denotes inter-planar spacing and h, k, and l represent the crystal plane's Miller indices.

The crystallite size(D) calculated by Williamson-Hall method [24]. According to this method, x-ray diffraction peak broadening FWHM (β_{hkl}) is written as

$$\beta_{hkl} = \beta\text{size} + \beta\text{strain} \tag{2}$$

This relation can be modified by

$$\beta_{hkl} = \frac{0.94\lambda}{DCos\theta} + 4\varepsilon\ tan\ \theta$$

$$\text{or, } \beta_{hkl}\ Cos\ \theta = \frac{0.94\lambda}{D} + 4\varepsilon\ Sin\ \theta$$

$$\text{or, } \beta_{hkl}\ Cos\ \theta = \varepsilon(4\ Sin\ \theta) + \frac{0.94\lambda}{D} \tag{3}$$

Where β_{hkl}, λ, D and ε are full width at half maximum, the wavelength of Cu-K_α radiation, crystallite size, and micro strain of the prepared samples respectively. Here

The X-ray density (ρ_x) was derived using the following equation [25]:

$$\rho_x = \frac{8M}{N_A a^3} \tag{4}$$

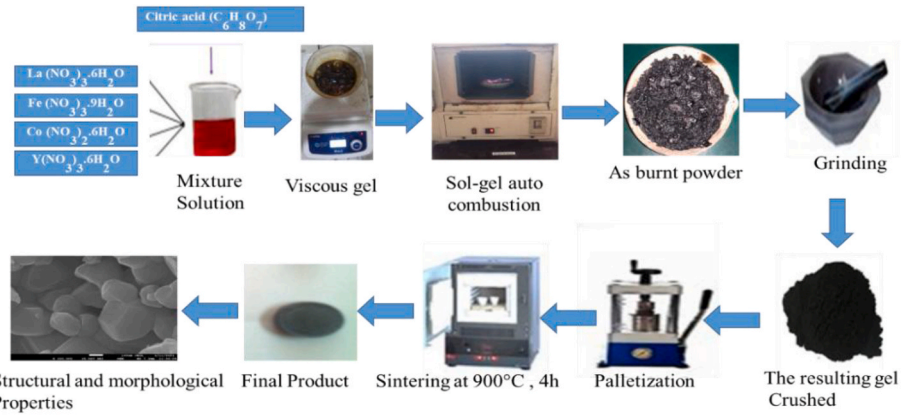

Fig. 1. Schematic diagram for the synthesis of Y^{3+} and La^{3+} doped Cobalt ferrite nanoparticles by sol-gel auto combustion process.

where M, N_A and a represents molecular weight, Avogadro's number, and lattice constant of the materials respectively. The bulk density of the synthesized samples was calculated by the following relation:

$$\rho_b = \frac{m}{\pi t r^2} \tag{5}$$

where m is mass (gm), r is radius and t is thickness of the prepared pallet samples.

And the porosity of the sample was measured by the following equation

$$P(\%) = \left(1 - \frac{\rho_b}{\rho x}\right)\% \tag{6}$$

Where ρx is X-ray density and ρb is bulk density of the prepared samples.

Tetrahedral Site radii r_A (Å) and octahedral site radii r_B (Å) are calculated by the following equation [26].

$$r_A\left(\overset{\circ}{A}\right) = (u - 0.25)a\sqrt{3} - R_0 \tag{7}$$

$$r_B\left(\overset{\circ}{A}\right) = (0.625 - u)a - R_0 \tag{8}$$

where u, a, and Ro are represented oxygen positional parameter, lattice parameter and oxygen ion radius respectively. The FTIR spectra of synthesized samples were recorded utilizing a Fourier Transform Infrared (FTIR, PerkinElmer) in the frequency region of 350–600 cm^{-1}.The force constants of the tetrahedral site (K_t) and octahedral site (K_O) are derived by using the following equation [27].

$$K_o = 0.942128 \times \frac{M\nu_2^2}{M + 32} \tag{9}$$

$$K_t = 2^{1/2} K_o \frac{\nu_1}{\nu_2} \tag{10}$$

where M, ν_1, and $\nu_2$are the molecular weight of prepared samples, the vibration frequency for tetrahedral and octahedral sites, respectively. The FE-SEM images and EDX spectrum of the synthesized samples were taken by Field-Emission Scanning Electron Microscopy (FE-SEM; JSM-7610F, Japan). A Vibrating Sample Magnetometer (VSM; EV-6, Microsence) was used to evaluate magnetizations versus applied magnetic field curves (M − H hysteresis) at room temperature. The anisotropy constant (K) was calculated by the following formula [9].

$$K = \frac{HcMs}{0.98} \tag{11}$$

where Hc and Ms are coercivity and saturation magnetization respectively.

The squareness ratio (R^2) and Bohr magnetization (η_B) in magnetic moment were determined by using the following formula

$$R^2 = \frac{Mr}{Ms} \tag{12}$$

$$\eta_B = \frac{MMs}{5585} \tag{13}$$

where Mr is the remanent magnetization, Ms saturation magnetization and M is molecular weight for the prepared sample.

Room-temperature dielectric properties was determined by High Precision Impedance Analyzer (4294A, Agilent) where applied the frequency range 100Hz to 110 MHz.The silver paste was employed on both sides of the prepared samples to enhance electrical conductivity.

The dielectric constant (έ) of the synthesized samples have been derived by using the formula

$$\acute{\varepsilon} = \frac{Cd}{\mathcal{E}_0 A} \tag{14}$$

where $\mathcal{E}_0$ is the permittivity at the free space, A is the cross-sectional area, C is the capacitance of the circular-shaped pellets, and d is the thickness of the pellet samples. At room temperature, Diffuse reflectance spectroscopy (DRS) of the materials was undertaken to use an UV-VIS-NIR spectrometer (UV-2600, Shimadzu).

3. Results and discussion

3.1. Structural analyses

The identification of the crystal phase for $CoY_{0.5x}La_{0.5x}Fe_{2-x}O_4$ nanoparticles with a series of x = 0.00 to 0.10 was accomplished by the XRD technique were shown in Fig. 2(a). The observed diffraction peaks of the XRD pattern of prepared samples were matched with the standard JCPDS Card No. 00-022-1086 and 01-082-8578 where CuKα ($\lambda = 1.540562$ Å) was used as X-ray source radiation. Bragg's peaks are noticed at 18.33°, 30.16°, 35.64°, 37.21°, 43.22° 53.54°, 57.02° and 62.71° corresponding to the crystal planes of (111), (220), (311), (222), (400), (422), (511), and (440) respectively. The appearance of all the diffraction peaks of synthesized nanoparticles ensures the formation of the cubic inverse spinel structure and the * sign indicates the mixed impurity phase of $LaFeO_3$. For higher concentrations (x = 0.06 to 0.10), owing to the larger ionic radius of Y^{3+}(0.95 Å), La^{3+}(1.06Å) than Co^{+2} (0.78Å) and Fe^{+3} (0.67 Å), excess Y^{3+} and La^{3+} cannot get into the crystal lattice, pile up at the grain boundaries as a secondary phase. There is a solubility limit for the replacement of Fe^{3+}ions by La^{3+} ions for its larger ionic radius. As a result, the numbers of Fe^{3+}ions that can be replaced byLa^{3+} ions are constrained. Thus, it is anticipated that $LaFeO_3$ phase will form along the grain boundaries as a result of an excess replacement of La^{3+} ions found similar observation in Ref. [9].

The crystallite sizes were calculated by the Williamson-Hall method using equation 2, and 3 and given in Table 1 and the W–H plots of $\beta\ cos\ \theta$ versus 4 $sin\ \theta$ for the synthesized samples are shown in Fig. 2(b). A linear plot provides the intercept from which the crystal size (D) was calculated, and the strain value was obtained from the straight-line fitting of the slope. It is observed that crystallite sizes of $CoY_{0.5x}La_{0.5x}Fe_{2-x}O_4$ decreased than pure cobalt ferrite due to difference in ionic radii of doped ions and replaced ions from the interstitial sites and the results matches with ref. [8,9,28,29]. The specific surface area (S) was calculated by $(S) = \frac{6}{D\rho_x}$, here D is crystallite size, and ρ_x is X-ray density. The calculated specific surface areas were 9.12 m^2/gm, 20.54 m^2/gm,16.77 m^2/gm,19.01 m^2/gm,14.48 m^2/gm and 17.41 m^2/gm for x = 0.00,0.02,0.04,0.06, 0.08 and 0.10, respectively.

The lattice parameters were calculated from XRD by equation (1) and Rietveld Refinement using Profex software. The lattice

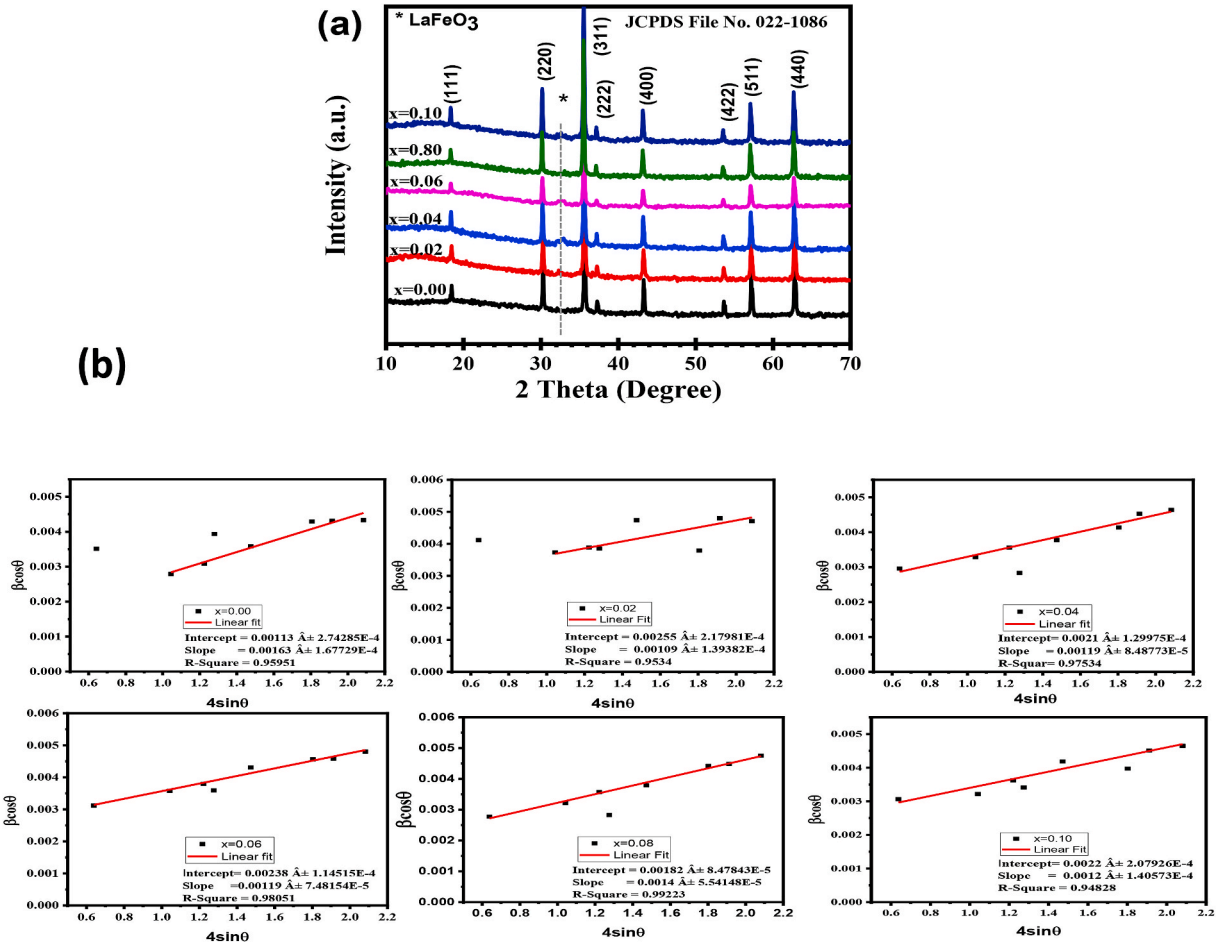

Fig. 2. (a) X-ray diffraction patterns and (b) Williamson and Hall (W–H) plots of $CoY_{0.5x}La_{0.5x}Fe_{2-x}O_4$ nanoparticles with different compositions x = 0.00–0.10.

Table 1
Structural parameters of synthesized $CoY_{0.5x}$ $La_{0.5x}Fe_{2-x}O_4$ferrite (where x = 0.00, 0.02, 0.04, 0.06, 0.08 and 0.10) nanoparticles sintering temperature at 900 °C.

Value of x	Lattice parameter a (Å)		Crystallite size D nm ±1	Micro strain $\varepsilon \times 10^{-3}$	X-ray density (gm/cm^3) ±0.0005	Bulk density (gm/cm^3) ±0.0005	Porosity (%) ±0.0005	Tetrahedral site radii r_A (Å) ±0.0005	Octrahedral site radii r_B (Å) ±0.0005
	From XRD Data ±0.0005	Rietveld Refinement ±0.0005							
x = 0.00	8.327	8.382	122	1.63	5.39	1.77	68.27	0.5693	0.7117
x = 0.02	8.332	8.383	54	1.09	5.41	2.13	60.62	0.5705	0.7130
x = 0.04	8.342	8.384	66	1.19	5.42	2.23	58.85	0.5727	0.7154
x = 0.06	8.346	8.385	58	1.19	5.44	2.38	56.25	0.5737	0.7164
x = 0.08	8.352	8.384	76	0.14	5.45	2.57	52.84	0.5750	0.7178
x = 0.10	8.357	8.386	63	1.2	5.47	2.61	52.28	0.5761	0.7191

parameter showed increasing behavior, which is attributed to the difference in the ionic radii of doped ions (Y^{3+} = 0.90 Å and La^{3+} = 1.16 Å) and replaced ions (Fe^{3+} = 0.645 Å) from the interstitial sites. The increasing lattice constant follow Vegards law [8] and similar observations were also reported by Refs. [9,29]. The X-ray density (ρ_x), bulk density (ρ_b) and porosity (*P%)* of the prepared samples were calculated by equations (4)–(4)–(6) respectively. It is observed that the ρ_x and ρ_b rise with rising doping concentration due to presence of the pores which mainly rely on sintering conditions. On the other hand, the percentage of porosity losses with a rise in Y^{+3} and La^{3+} content which may be due to increase balk density. The tetrahedral site radii (r_A) and octrahedral site radii (r_B) were calculated using equations (7) and (8) respectively [Table 1]. From Fig. 2(b), the slope of the plot was contained positive. The calculated strain values show that the as-prepared samples have a positive strain value, which is indicative of the presence of tensile strain. The structural parameters of cobalt ferrite by adding either lanthanum or yttrium were examined by several researchers [8,9,28, 29], but here our study both La^{3+} and Y^{3+} was doped together. In this research revealed that the prepared samples had increased lattice parameters and density but decreased crystallite sizes, porosity and micro strain than cobalt ferrite.

Tetrahedral bond length (d_{AX}), octahedral bond length (d_{BX}), tetrahedral edge (d_{AXE}), shared octahedral edge (d_{BXE}) and unshared octahedral edge (d_{BXEU}) were calculated using investigational values of lattice parameter (a) and Oxygen positional parameter U (u = 0.381 Å) [26]. The structural parameters values are $d_{AX,}$ d_{BX}, d_{AXE}, d_{BXE} and d_{BXEU} of $CoY_{0.5x}La_{0.5x}Fe_{2-x}O_4$nanoparticles tabulated in Table 2 d_{AX} and d_{BX} are the shortest distance between A-site cations and B-site cations, respectively. It is seen that the tetrahedral edge and octahedral edge follow an increasing trend with increasing dopant concentrations. This is often ascribed to the rise in lattice constant with an increase in Y^{3+} and La^{3+} content in the samples.

3.2. Fourier Transform Infrared spectroscopy (FTIR) analysis

The FTIR study detected the prepared sample's behavior as determined by the absorption band frequencies. In the case of inverse spinel ferrites, the frequency range between 350 and 600 cm^{-1} was generally studied. The FTIR spectra (T%) of the ferrite samples predominately form two frequency peaks at the tetrahedral site (A-site) and octahedral site (B-site), which is attributed to the stretching vibrancy of metallic-oxygen ions at the interstitial sites.

The formation of the higher absorption peak ν_{11} (592–597 cm^{-1}) and the lower absorption peak ν_{22} (395-401 cm^{-1}) corresponds to the stretching vibrations of Fe^{2+}-O ions at the tetrahedral (A) site and the octahedral (B) site, respectively, as shown in Fig. 3. The synthesized nano-ferrites show a cubic inverse spinel structure formed in the range of the absorption peak mentioned [30]. The FTIR spectrum also shows the presence of moisture. Moreover, the frequency peak around 1639 cm^{-1} arises from the absorbed water and atmospheric Co_2. The absorption peaks around 1600–3500 cm^{-1} are assigned for the adsorbed water molecule, representing the O–H stretching and H–O–H bending modes of vibration, respectively. Besides this, absorption peaks arise at1129 cm^{-1} attributed to the deformation of the C–H group [31]. The tetrahedral force constant (K_t) and octahedral force constant (K_O) were calculated by equations (9) and (10) and presented in Table 2. It is well known that the bond length is inversely proportional to the force constant. K_t and K_O decrease with an increase in doping concentrations, which has been attributed to the variation in cation–oxygen bond lengths at the A and B-sites [32]. The A-site bond length (A-O) is smaller than the B-site bond length (B–O). This is because the covalence of the tetrahedral site bond A–O is higher than that of the octahedral site bond B–O.

3.3. Field Emission Scanning Electron Microscopy (FESEM) analysis

The microstructure of $CoY_{0.5x}La_{0.5x}Fe_{2-x}O_4$ exhibits normal grain growth and a relatively uniform and homogeneous distribution, as shown in Fig. 4(a–f). It was noticed that undoped cobalt ferrite x = 0.00 showed well-faceted grains with no agglomeration, but Y^{3+} and La^{3++}doped cobalt ferrite x = 0.08 and x = 0.10 nanoparticles' grain was spherical with a little agglomeration. The agglomeration of grain structure was due to the calcinations process, magnetic nature, and small crystallite size [33]. The structure is consolidated when the grains are gathered and the clusters are elevated because the magnetic force and weak Vander wall bonds play a significant role in retaining these aggregates in the samples [34].

The average grain size was calculated by Image J software and distribution curve was presented with FE-SEM in Fig. 4(a–f). The grain size distribution of Cobalt ferrite particles is uniform in all cases. The average grain sizes of the prepared samples are approximately 137 nm, 102 nm, 98 nm, 82 nm, 63 nm, and 52 nm for x = 0.00, 0.02, 0.04, 0.06, 0.08, and 0.10, respectively. Gain sizes were reduced systemically with composition due to larger atomic sizes (Y^{3+} and La3^{+}) and Vander Wall forces [11]. SEM images revealed

Table 2
Structural parameters: hopping length tetrahedral site (L_A), hopping length Octahedral site (L_B), bond length (d_{AX} and d_{BX}), tetrahedral edge (d_{AXE}), sheared octahedral edge (d_{BXE}), un-sheared octahedral edge (d_{BXEU}), absorption bands tetrahedral sites (ν_1)and octahedral sites (ν_2), tetrahedral sites force constant (K_t) and octahedral sites force constant (K_0) of $CoY_{0.5x}La_{0.5x}Fe_{2-x}O_4$nanoparticles.

Value of x	L_A (Å)	L_B (Å)	d_{AX} (Å)	d_{BX} (Å)	d_{AXE} (Å)	d_{BXE} (Å)	d_{BXEU} (Å)	ν_1 Cm^{-1}	ν_2 Cm^{-1}	$K_t \times 10^5$ (dynes/ Cm^{-2})	$K_0 \times 10^5$ (dynes/ Cm^{-2})
x = 0.00	3.6056	2.9443	1.8893	2.0332	3.0853	2.8027	2.9457	597	401	1.33	2.80
x = 0.02	3.6078	2.9458	1.8905	2.0342	3.0872	2.8044	2.9475	596	400	1.32	2.79
x = 0.04	3.6123	2.9493	1.8927	2.0366	3.0909	2.8077	2.9510	595	399	1.32	2.78
x = 0.06	3.6139	2.9507	1.8936	2.0376	3.0923	2.8091	2.9524	594	397	1.31	2.76
x = 0.08	3.6165	2.9528	1.8950	2.0391	3.0946	2.8111	2.9545	593	396	1.31	2.75
x = 0.10	3.6186	2.9546	1.8961	2.0403	3.0964	2.8128	2.9563	592	395	1.29	2.74

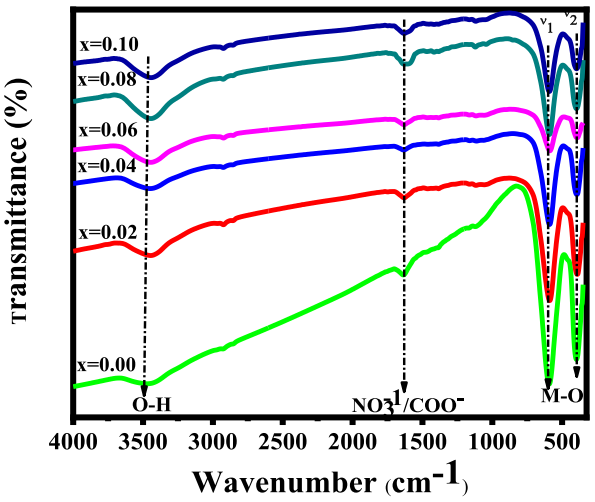

Fig. 3. FTIR spectra of $CoY_{0.5x}La_{0.5x}Fe_{2-x}O_4$ nanoparticles with different compositions x = 0.00–0.10.

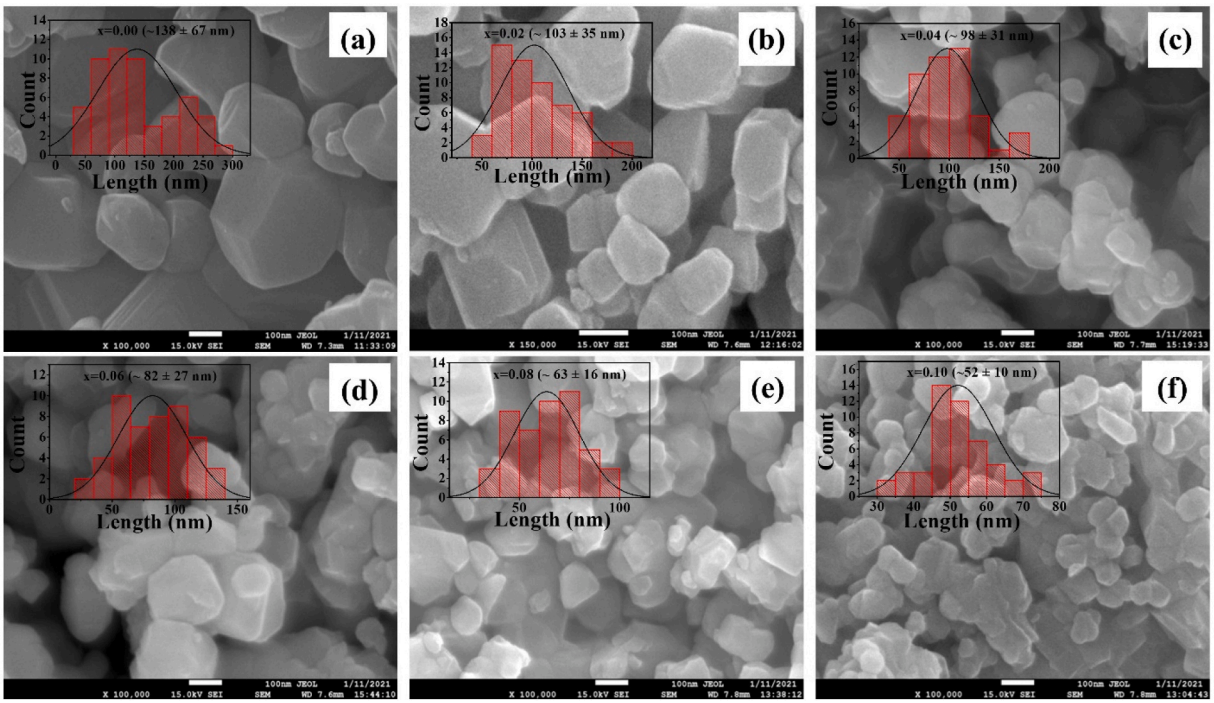

Fig. 4. FE-SEM micrographs and the grain size distribution curves of $CoY_{0.5x}La_{0.5x}Fe_{2-x}O_4$ nanoparticles with different compositions: (a) x = 0.00; (b) x = 0.02; (c) x = 0.04; (d) x = 0.06; (e) x = 0.08 and (f) x = 0.10.

that the grains are at the nano scale with vivid pores which is more suitable to the gas sensing applications because smaller grains have larger specific surface area [35].

The energy dispersive X-ray analysis (EDX) spectra of pure Cobalt ferrite (x = 0.00) and Y^{3+} and La^{3+} doped Cobalt ferrite (x = 0.10) nanoparticles correspond to the elements Co, Y, La and Fe were presented in Fig. 5(a and b) and it represent that Y^{3+} and La^{3+}ions exist in synthesized samples.

3.4. Room-temperature magnetic properties

At room temperature, the magnetic properties of $CoY_{0.5x}La_{0.05x}Fe_{2-x}O_4$ nanoparticles (where x = 0.00, 0.02, 0.04, 0.06, 0.08, and 0.10) were investigated by Vibrating Sample Magnetometer (VSM). Fig. 6(a) depicts the M − H loop of Y^{3+} and La^{3+} doped Cobalt

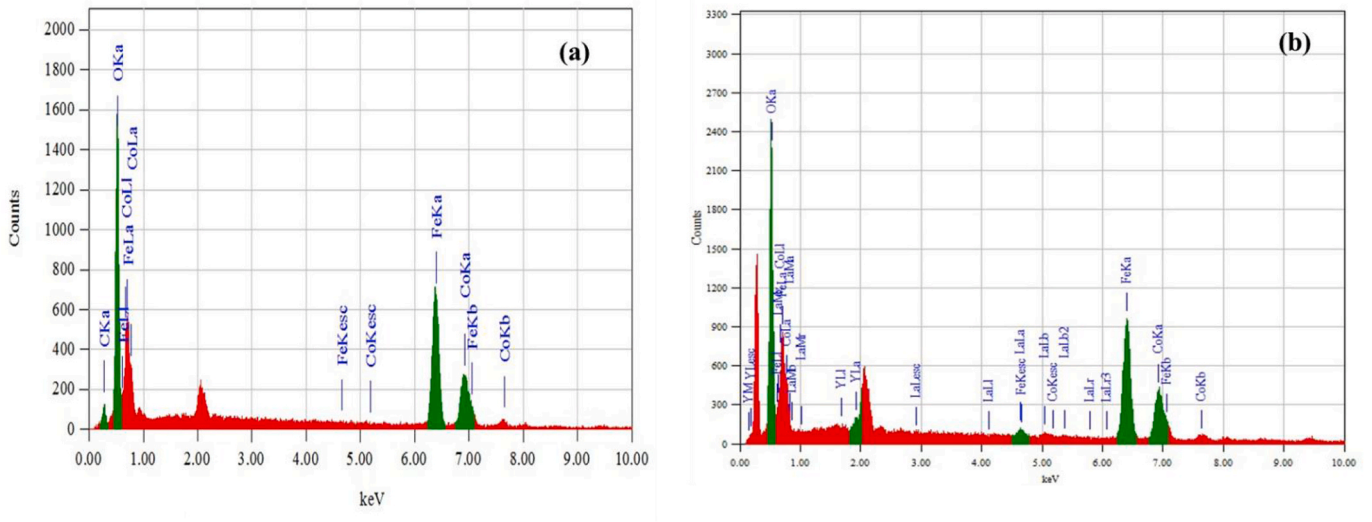

Fig. 5. EDX spectra of the synthesized $CoY_{0.5x}La_{0.5x}Fe_{2-x}O_4$ nanoparticles with compositions (a) x = 0.00 and (b) x = 0.10.

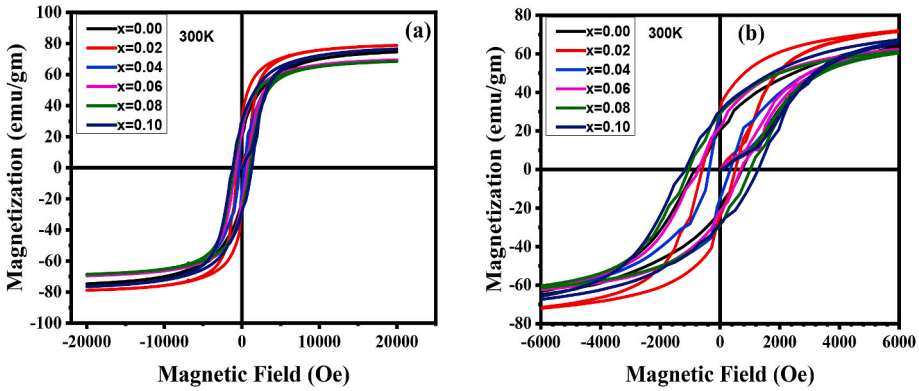

Fig. 6. (a) Room temperature Hysteresis (M–H) curve of the Co $Y_{0.5x}$ $La_{0.5x}$ Fe_{2-x} O_4 (x = 0.00, 0.02, 0.04, 0.06, 0.08 and 0.10) nanoparticles and (b) is magnified view of the M − H curve of (a).

ferrite nanoparticles plotted with an applied magnetic field of ±20000 Oe. The S-shaped hysteresis loops were observed in Fig. 6(a and b), which indicates the soft magnetic nature of the prepared samples.

The magnetic properties of ferrite nanoparticles like saturation magnetization (Ms), remanence magnetization (Mr), squareness value (R^2), coercivity (Hc), and Bohr magnetization (η_B) have been influenced by several factors such as chemical composition, synthesis techniques, density, grain growth, A-B exchange interaction, and anisotropy [36]. Table 3 contains data on magnetic properties and it is shown that the saturation magnetization varied from 68 emu/g to 78 emu/g with the increase in Y^{3+} and La^{3+}doping concentrations in cobalt ferrite nanoparticles. The saturation magnetization of pure cobalt ferrites is 74 emu/g.The doping concentration x = 0.02 was obtained minimum crystallite size and highest saturation magnetization. The anomalous behavior of Ms can be explained on the basis of crystallite size, grain size, and coercivity [37]. The magnetic saturation parameters can be influenced by both internal (composition) and external (micro structural) factors. This phenomenon can be explained on the basis of Néel's sub-lattice model [38] and the exchange interactions between Fe^{3+} ions and substituted ions at the interstitial sites of the crystal lattice, such as the tetrahedral site (A-site) and the octahedral site (B-site). Generally, the octahedral site is occupied by rare earth ions due to their larger ionic radius, whose magnetic moment is created by 4f electrons located there. At room temperature, the rare earth ion's magnetic dipole moment stays disorganized and randomly generated, and consequently, Y^{3+} and La^{3+}ions can be taken into account as non-magnetic ions contributing zero magnetic moment [37]. From Néel's two-sublattice model [38], the magnetic moment per formula unit is determined by $\eta_B = M_B\text{-}M_A$, the magnetic moments of the A and B sites are M_A and M_B, respectively. The magnetic moments of Co, Y, La and Fe are $3\mu_B$, $0\mu_B$, $0\mu_B$and $5\mu_B$respectively.It is evident that non-magnetic rare earth ions occupy octahedral sites; the μ_B decreases in the cation distribution model; and the A-B interactions are stronger than the A-A and B–B interactions [39]. The calculated $\eta_B = 3.0\mu_B$, $2.90\mu_B$, $2.80\mu_B$, $2.70\mu_B$, $2.60\ \mu_B$ and $2.50\mu_B$ for x = 0.00,0.02, 0.04, 0.06, 0.08 and 0.10 respectively.

The coercivity (Hc), anisotropy constant (K), squareness ratio (R^2) and Bohr magnetization (η_B) in magnetic moment are calculated using equations (11)–(11)–(13) and tabulated it Table 3. At first, the coercivity (Hc) decreases from 740 Oe to 342 Oe for doping concentration x = 0.000 to 0.04 and again it increases from 702Oe to 1278 Oex = 0.066 to 0.10. It may be due to enough defects or porosity in the sample, which is in agreement with M. A. Amessier et al. [17]. The Hc is affected by a variety of factors such as size, defects, porosity, microstrain, the preferred site occupancy of various ions and ionic radii of rare earth, magnetic moment, magneto-crystalline anisotropy, and so on [40]. On the otherh and, Hc varies inversely withthe grain size of the nanoparticles. It was observed that the maximum Hc (1286 Oe) and minimum grain size (52 nm)were obtained for the doping concentration x = 0.10. So, the increased coercivity with Y^{3+} and La^{3+} substitutions could be attributed to grain size reduction.

It was observed that that the anisotropy constant varies from 24.59 erg/g to 101 erg/g, squareness ratio 0.272 to o.421 and magnetic moment $2.92\mu_B$–$3.33\mu_B$ which is related to saturation magnetization and coercivity value. The squareness ratio $R^2 = \frac{Mr}{Ms} < 0.5$ for all samples, which indicates that Cobalt ferrite and Y^{3+} and La^{3+} doped cobalt ferrite issuparpamagnetic state [37].

Table 3
Saturation magnetization (Ms), Remanence magnetization (Mr), Coercivity (Hc), Squareness value (Mr/Ms), CoercivityHc, Anisotropy Constant (K) and Bohr Magneton (η_B) for Co $Y_{0.5x}$ $La_{0.5x}$ $Fe_{2-x}O_4$ ferritenanoparticles.

Value of x	Saturation Magnetization Ms (emu/g)	Remanent Magnetization Mr (emu/g)	Squareness value (Mr/Ms)	CoercivityHc (Oe)	Anisotropy Constant K × 10^3 (erg/g)	Bohr Magneton (η_B) (μ_B)
x = 0.00	74.55	20.27	0.272	740	57.46	3.13
x = 0.02	78.90	30.27	0.384	515	42.32	3.33
x = 0.04	69.04	27.74	0.402	342	24.59	2.92
x = 0.06	69.46	21.91	0.315	702	50.79	2.96
x = 0.08	68.56	28.85	0.421	1016	72.55	2.93
x = 0.10	76.61	30.24	0.394	1278	101.98	3.29

3.5. Room-temperature dielectric properties

The dielectric study gives information on the crystal structure, charge storage capacity, grain boundary, and transport properties of dielectric material [41]. The real dielectric constant (έ) of $CoY_{0.5x}La_{0.5x}Fe_{2-x}O_4$ (x = 0.00, 0.02.0.04, 0.06, 0.08, 0.10) at room temperature in the frequency range 100Hz to 110 MHz have been derived by using equation (14). The variation of the dielectric constant as a function of frequency for all the samples is shown in Fig. 7(a). The value of έ depends on factors such as preparation method, sintering temperature, grain size, density, porosity, and surface homogeneity [42]. The dielectric constant of all the samples shows a higher value at the lower frequency region; as the frequency rises, the έ decreases and becomes constant at a specific frequency, indicating the typical ferromagnetic behavior without any unusual peak. This behavior in the dielectric constant is associated with the Maxwell-Wagner type of interfacial polarization in agreement with Koop's phenomenological theory [43]. According to this model, the dielectric constant is attached to dipolar, electronic, ionic, and interfacial polarization, influencing the dielectric properties. Grain boundaries are much effective at low frequency, but when at high frequency, the grains become highly conducting into action, due to which the dielectric constant decreases. The obtained έ values systematically increased from 74.68 to 149.31 for all the samples. Primarily, when the electric field is applied to the samples, the electrons follow the field and pile up at the grain boundaries through hopping, which produces polarization. But upon a particular frequency, the electron exchange between Fe^{2+}/Fe^{3+} ions cannot follow the field that causes the decrease in polarization. As a result, the έ decreases with the increasing frequency of the applied field. From our data, it can be inferred that Y^{3+} and La^{3+}doped cobalt ferrites tend to vary significantly, improving the nano ferrites for microwave frequency applications.

At room temperature, the change of dielectric loss (tanδ) of $CoY_{0.5x}$ $La_{0.5x}$ $Fe_{2-x}O_4$ nano particles with frequency has depicted in Fig. 7(b). It is noticed that the tanδ reduces with an increase in frequency which exhibits normal dielectric behavior for Y^{3+} and La^{3+} doped $CoFe_2O_4$ nanoparticles. At low frequency regions, the tanδ reduces directly but with the rise in frequency, the tanδ value reduces until attaining a certain point where the value of tanδ remains constant for all samples. This attitude is observed because of the grain boundary effect, which needs more energy to interchange electrons between Fe^{2+} and Fe^{3+} ions [44]. However, the dielectric loss reduces at higher-frequency areas which could be attributed to the inability of domain wall motion with the fast change of applied AC field.

The room temperature frequency dependence AC conductivity (σ_{ac}) of $CoY_{0.5x}$ $La_{0.5x}$ $Fe_{2-x}O_4$ (where x = 0.00, 0.02, 0.04, 0.06, 0.08, 0.10) nano particles are demonstrating in Fig. 7©. The AC conductivity displayed a rising tendency with the rise in frequency for all the samples. The σ_{ac} of ferrites is increase with frequencies which is narrated by Koop's two-layer model and the space charge [43]. The conduction mechanism in spinel ferrites is due to the hopping between ions with mixed valence. It is clear that the doping of Y^{3+} and La^{3+} ions in $CoFe_2O_4$ ferrites improves the ac conductivity and also corroborations the mechanism for the improvement in the dielectric constant and corresponds with the report in R. S. Yadav et al. [26].

Impedance spectroscopy is a well-known technique to explore the electrical response of ceramic materials as a function of frequency, whose properties depend on their ceramic quality and the impedance of electrodes, the distribution of dopants, and grain and grain boundary performances [45]. This technique also reports on imaginary and real parts of the impedance substance of a material. This analysis is mainly used to fit the impedance data into an equivalent circuit representing the material under investigation. The Nyquist plot states the whole performance of grain and grain boundary resistance.

Fig. 8 (a) illustrates the change of the real part of impedance (Z′) as a function of frequency. It is observed that Z′ reduces gradually with the increase in frequency, which indicates the discharge of space charges as a result of a reduction in the interruption characteristics of the material. Besides, a rise in conduction with frequency suggests that the ferrites be treated as a semiconductor material [46].

Fig. 8(b) shows the frequency versus imaginary impedance (Z″) at room temperature for all prepared samples. It is observed that the imaginary impedance reduces with increased employed frequency and remains low it at high frequency. This plot expresses relaxation peaks owing to space charge relaxation, which is attached to charge carriers resulting from energy vacancies [47].

A Nyquist plot for unfitted and fitted data with an equivalent circuit for $CoY_{0.5X}$ $La_{0.5X}$ $Fe_{2-x}O_4$ nanoparticles was shown in Fig. 9, at a frequency range of 40 Hz to 110 MHz.These plots were fitted to an equivalent circuit with the help of Zsimp Win software, and the data obtained from the fittings were tabulated in Table 4. One semicircle was successfully displayed by an equivalent circuit model (R_1, Q_1) and (R_2, Q_2) where R_1 and R_2 are the grain resistance and grain boundary resistance, respectively, and Q_1 and Q_2 are constant phase elements for grain and grain boundary, which are capacitive parameters. Non-ideal Debye-like behavior of the capacitance, $C = R^{1-n/n} Q^{1/n}$, where the value of n is 1 for pure capacitance and zero for pure resistance behavior. The table showed that the grain exhibited ideal capacitance behavior and the grain boundary exhibited non-ideal capacitance behavior due to the presence of relaxation process with the same relaxation time or disorder in the grain boundary. From Table 4, the grain resistance and grin boundary resistance were found to drop in magnitude with the increasing doping concentration. Fig. 9 showed no complete semicircle for the samples x = 0.00, 0.02, and 0.06, expressing that the grain boundary impedance was outside the measurement scale. This may be owing to the presence of some extra time constant, that appears beyond the surveyed frequency range. Semicircle shapes were observed for x = 0.08 and x = 0.10 samples in the high frequency region because the grain and grain boundary contributions were superior to the grain contributions [48]. Moreover, it was noticed that the value of Z′ and Z″ in the spectra reduces with increasing doping concentration, suggesting that the net resistance of the Co $Y_{0.5x}$ $La_{0.5x}$ Fe_{2-x} O_4 nanoparticles falls consistently.

3.6. Optical properties

UV–Visible spectroscopy is an important tool to thoroughly examine the optical energy gaps of nanoparticles. Diffuse reflectance

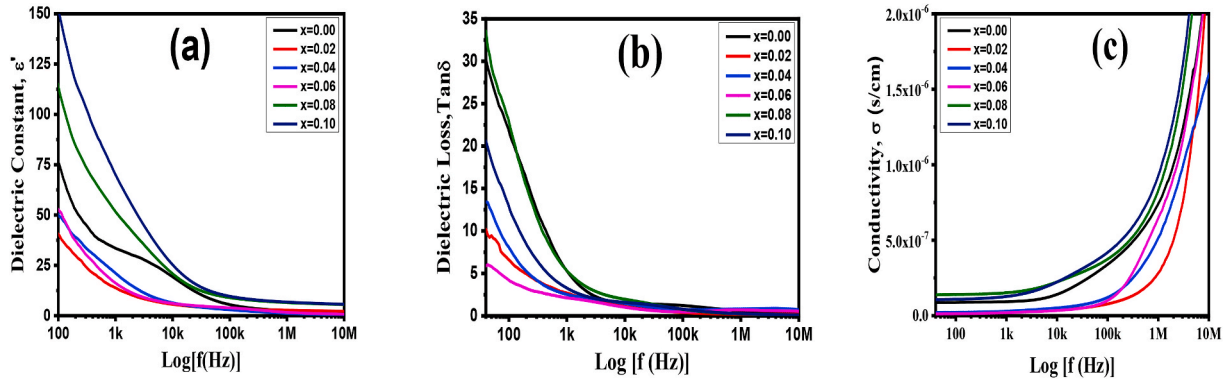

Fig. 7. (a) Variation of dielectric Constant (έ), (b) Variation of dielectric loss (tanδ) and (c) Variation of AC conductivity (σ_{ac}) of the $CoY_{0.5x}La_{0.5x}Fe_{2-x}O_4$ nanoparticles at room temperature.

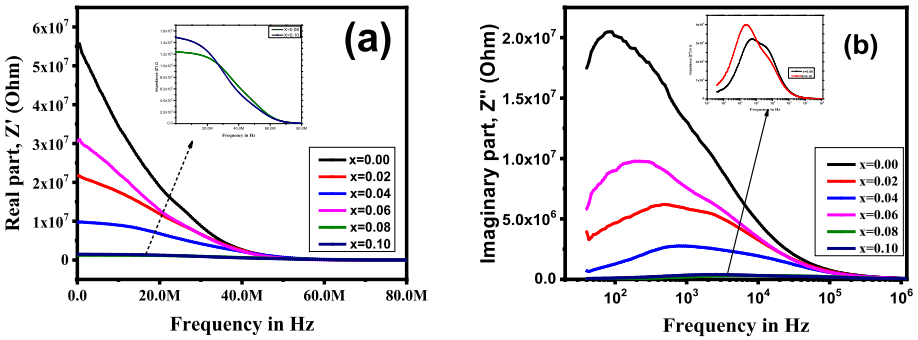

Fig. 8. (a). The real part of impedance (Z′) of the Co $Y_{0.5x}$ $La_{0.5x}$ Fe_{2-x} O_4 nanoparticles with frequency (inset: The real part of impedance (Z′) for x = 0.08 and x = 0.10) and (b) the imaginary part of impedance (Z′′) of the Co $Y_{0.5x}La_{0.5x}$ Fe_{2-x} O_4 nanoparticles with frequency (inset: The imaginary part of impedance (Z′) for x = 0.08 and x = 0.10) at room temperature.

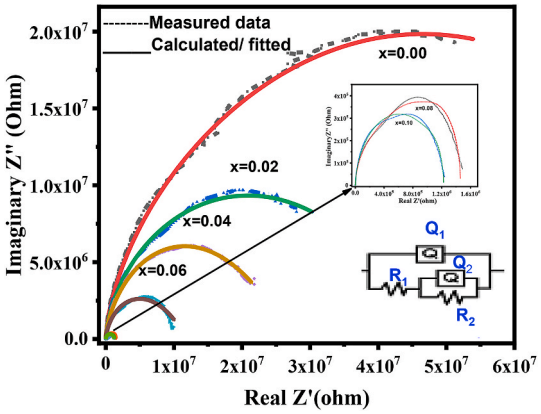

Fig. 9. Nyquist plot with fitting curvesof the Co $Y_{0.5x}$ $La_{0.5x}$ Fe_{2-x} O_4 nanoparticles (Inset: Nyquist plot with fitting curves for x = 0.08 and x = 0.10 and equivalent circuit for the best-fitted).

spectroscopy (DRS) of Y^{3+} and La^{3+} doped $CoFe_2O_4$was studied within the wavelength range of 220–1400 nm by a UV–Vis–NIR spectrometer and analyzed data was presented in Fig. 10. The UV–Vis reflectance data for al samples are converted to absorption through Kubelka-Munk's theory. The Kubelka-Munk function is straight proportionate to the absorption coefficient (α), measured usingthis relation $F(R_\alpha) = \frac{(1-R_\alpha)^2}{2R_\alpha}$,here F (R_α) and R_α are the Kubelka -Munk function and diffuse reflectance respectively [49].

The UV absorption bands of $CoY_{0.5X}$ $La_{0.5X}$ $Fe_{2-x}O_4$ nanoparticles were found in the range of 300–600 nm for all the samples. It is conspicuous that synthesized powder nanoparticles have a broad absorption ranging from deep UV to visible part of the radiation

Table 4
Different parameters of the equivalent circuit components of Nyquist plot curve.

Value of x ($CoY_{0.5x}$ $La_{0.5x}$ $Fe_{2-x}O_4$)	Grain resistance R_1 (KΩ)	Grain Capacitance C_1 pF	n_1	Grain boundary resistance R_2 (KΩ)	Grain boundary capacitance C_2 pF	n_2
x = 0.00	103	1.763	1	99730	6.918	0.4523
x = 0.02	117	1.763	0.9986	26690	8.009	0.4718
x = 0.04	84	1.888	1	11670	14.07	0.4799
x = 0.06	40	3.534	0.9706	3683	20.89	0.4916
x = 0.08	17	6.450	0.9533	2796	25.65	0.4690
x = 0.10	13	7.599	0.9494	2191	39.22	0.5838

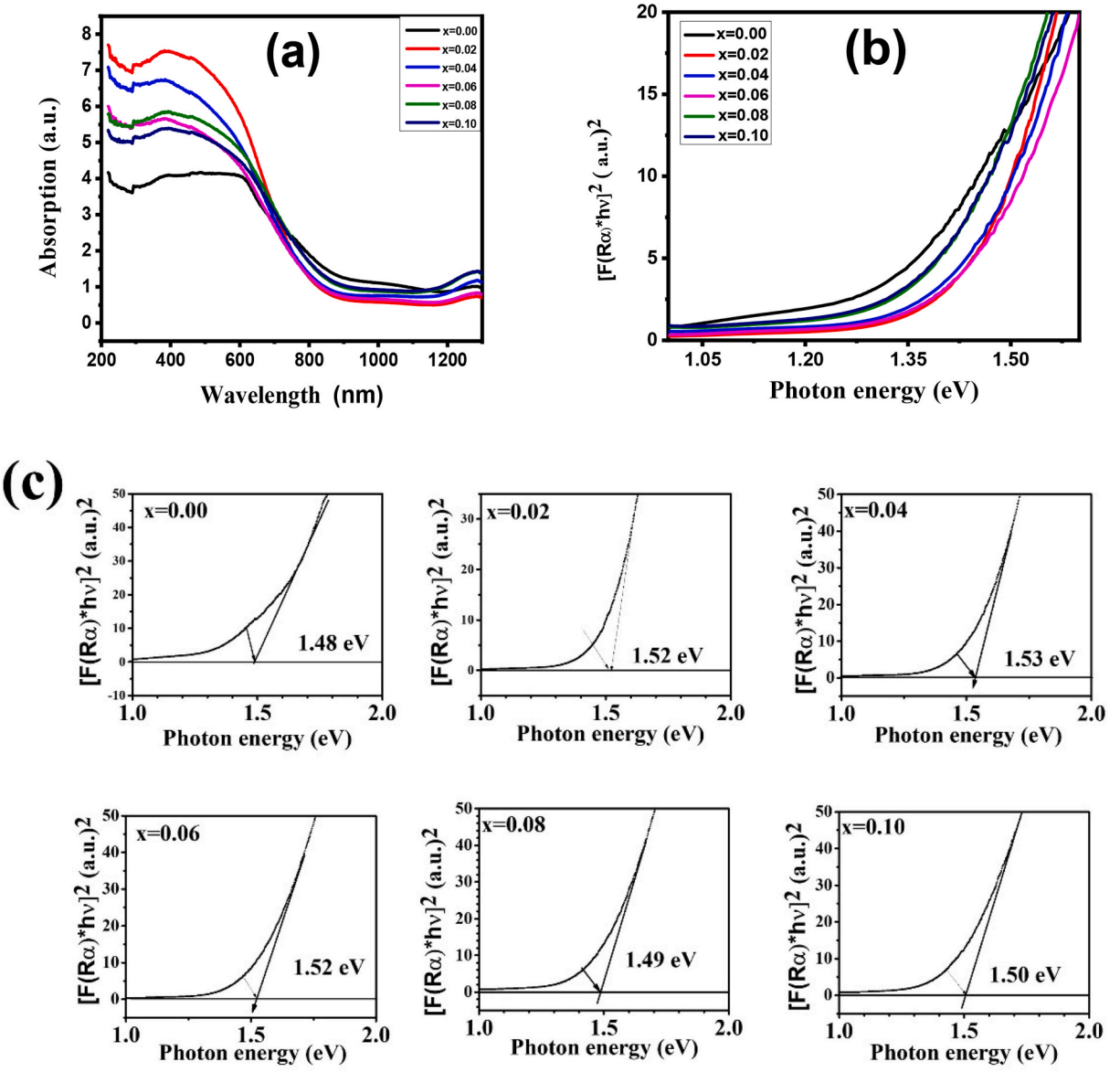

Fig. 10. (a)UV–Vis diffuse absorption spectra(b) and (c) Tauc plot of band gap energy of $CoY_{0.5x}$ $La_{0.5x}$ $Fe_{2-x}O_4$ ferrite nanoparticles.

which might have been connected to the quantum size effect, suggesting that they can be used as a photocatalyst. In Fig. 10(b) and (c) the optical band gap was identified at the intercept of the linear extrapolation with the X-axis. The band gap was calculated from the Tauc plot by $\left[h\nu F(R_\alpha)^{\frac{1}{n}}\right] \propto h\nu - E_g$,here α is absorption coefficient, E_g is the energy of the band gap, ν is Planck constant and h is the

frequency of the incident light [50]. The value of n = ½ is used for direct E_g and n = 2 is used for indirect E_g. The optical band gap was destined using the Tauc plot by extrapolating the linear part of the plot $h\nu F(R_\infty)^{\frac{1}{n}} = 0$.

The E_g obtained to be 1.48 eV, 1.53eV, 1.52 eV, 1.52 eV, 1.49 eV and 1.50 eV for x = 0.00, 0.02, 0.04, 0.06, 0.08, 0.10 respectively for $CoY_{0.5x}$ $La_{0.5x}$ $Fe_{2\text{-}x}O_4$ ferrite. Physically, there exist same conduction and valence bands in the direct band gap of the hole momentum and the electron. The direct Egfound1.48 eV described the electron requires 1.48 eV of energy to release a photon from the valence band to the conduction band. The value of Eg was increased with doping concentration than pure cobalt ferrite which might have been attribute to several causes like the presence of a little impurity, carrier density, crystal size and strain etc. [51], matched with the reports [9,17,30]. The band gap energy increases with decreasing grain sizes, consistent with FE-SEM and UV–Vis spectroscopy findings, suggested thatY^{3+} and La^{+3} improves optical properties.

4. Conclusion

$CoY_{0.5x}$ $La_{0.5x}$ $Fe_{2\text{-}x}O_4$ nanoparticles have been successfully synthesized by the sol-gel auto combustion process. Structural, magnetic, electrical, and optical properties of pure and doped $CoFe_2O_4$ were studied in detail. The XRD spectra expressed the single-phase cubic spinel structure with the crystallite sizes varying from 122 nm to 54 nm. The lattice parameters increased from 8.382 Å to 8.386 Å with increasing Y^{3+} and La^{+3} concentrations in cobalt ferrite as the radius of small ions was replaced by the radius of larger ions. FTIR spectra confirmed the presence of octahedral and tetrahedral sites and the metal-oxygen bond at 593 $cm^{-1}$to 597 cm^{-1} corresponding to the stretching M − O bond in the prepared samples. FE-SEM micrographs of synthesized samples showed well-defined grain growth while the grain size decreased from 137 nm to 52 nm. VSM study of synthesized ferrite exhibited soft ferrimagnetic nature, and the maximum H_c(~1276) was obtained for x = 0.10. The dielectric measurement such as dielectric constant, low dielectric loss, conductivity and impedance exhibits that samples were responsive to applied frequency. The dielectric constant is reduced at high frequencies as a common behavior of magnetic materials. The conductivity increases with an increase in Y^{3+} and La^{3+}concentration of the cobalt ferrite owing to an increase in the charge carrier mobility. It was observed from Nyquist plots that the conductivity of ferrite contributed by both grains and grain boundaries. The optical band gap energy counted from the Tauc plot, reveals the raising tendency with increasing doping concentration. The prepared ferrite nanoparticles with improved structural, magnetic, and dielectric properties suggested that these materials may be compatible for magneto-recording and high-frequency applications.

Acknowledgment

Bangladesh Council of Scientific and Industrial Research (BCSIR), Dhaka, Bangladesh.

References

[1] S.Y. Srinivasan, K.M. Paknikar, D. Bodas, V. Gajbhiye, Applications of cobalt ferrite nanoparticles in biomedical nanotechnology, Nanomedicine 13 (2018) 1221–1238, https://doi.org/10.2217/nnm-2017-0379.
[2] N. Khatun, M.S. Hossain, M.H.A. Begum, S. Islam, N.I. Tanvir, R.H. Bhuiyan, M. Al-Mamun, Effect of sintering temperature on structural, magnetic, dielectric and optical Properties of Ni-Mn-Zn- ferrites, J. Adv. Dielect. 11 (2021), 2150028, https://doi.org/10.1142/S2010135X21500284.
[3] V.S. Kumbhar, A.D. Jagadale, N.M. Shinde, C.D. Lokhande, Chemical synthesis of spinel cobalt ferrite ($CoFe_2O_4$) nano-flakes for super capacitor application, J. Appl. Sur. Sci. 259 (2012) 39–43, https://doi.org/10.1016/j.apsusc.2012.06.034.
[4] A. Kovalenko, R.S. Yadav, J. Pospisil, O. Zmeskal, D. Karashanova, P. Heinrichova, M. vala, J. Havlica, M. Weiter, Towards improved efficiency of bulk-heterojunction, Solar cells using various spinel ferrite magnetic nanoparticles, Org. Electron. 39 (2016) 118–126, https://doi.org/10.1016/j.orgel.2016.09.033.
[5] R.S. Priya, P. Chaudhary, E.R. Kumar, A. Balamurugan, Ch Srinivas, G. Prasad, B.C. Yadav, D.L. Sastry, Evaluation of structural, dielectric and electrical humidity sensor behavior of $MgFe_2O_4$ ferrite nanoparticles, Ceram. Int. 47 (2021) 15995–16008, https://doi.org/10.1016/j.ceramint.2021.02.174.
[6] M.S. Hossain, M.B. Alam, M. Shahjahan, M.H.A. Begum, M.M. Hossain, S. Islam, N. Khatun, M. Hossain, M.S. Alam, M. Al-Mamun, Synthesis, structural investigation, dielectric and magnetic properties of Zn^{+2} -doped cobalt ferrite by the sol–gel technique, J. Adv. Diel. 8 (2018), 1850030, https://doi.org/10.1142/S2010135X18500303.
[7] Le T. Lu, Ngo T. Dung, Le D. Tung, Cao T. Thanh, Ong K. Quy, Nguyen V. Chuc, Shinya Maenosonoe, Nguyen T.K. Thanh, Synthesis of mangnetic cobalt ferrite nanoparticles with controlled morphology, mono dispersity and composition: the influence of solvent, surfactant, reductant and synthetic conditions, Nanoscale 7 (2015) 19596–19610, https://doi.org/10.1039/c5nr04266f.
[8] K.L. Routray, S. Saha, D. Behera, Rare-earth (La^{3+}) substitution induced changes in the structural, dielectric and magnetic properties of nano- $CoFe_2O_4$ for high-frequencyand magneto-recording devices, Appl. Phys. A 125 (2019), https://doi.org/10.1007/s00339-019-2615-8.
[9] I.K. Punithavathy, A. Rajeshwari, S.J. Jeyakumar, N. Lenin, B. Vigneshwaran, M. Jothibas, B. Arunkumar, Impact of lanthanum ions on magnetic and dielectric properties of Cobalt nanoferrites, J. Mater. Sci. Mater. Electron. 31 (2020) 9783–9795, https://doi.org/10.1007/s10854-020-03523-3.
[10] S. Singhal, S.K. Barthwal, K. Chandra, XRD, magnetic and mössbauer spectral studies of nano size aluminum substituted cobalt ferrites ($CoAl_xFe_{2-x}O_4$), J. Magn. Magn Mater. 306 (2006) 233–240, https://doi.org/10.1016/j.jmmm.2006.03.023.
[11] K.H. Sharma, P. Sharma, Impurity effect of La on Co ferrite: synthesis and structural study, Optoelectr. Adv. Mater. Rap. Commun. 7 (2013) 887–890.
[12] D.R. Mane, D.D. Birajdar, S. Patil, S.E. Shirsath, R.H. Kadam, Redistribution of cations and enhancement in magnetic properties of Sol-gel Synthesized $Cu_{0.7\text{-}X}$ Co_x $Zn_{0.3}Fe_2O_4$ ($0 \leq X \leq 0.5$), J. Sol. Gel Sci. Technol. 58 (2011) 70–79, https://doi.org/10.1007/S10971-010-2357-8.
[13] S. K Gore, S.S. Jadhav, S.M. Patange, M. Naushad, R.S. mane, K.H. Kim, The structural and magnetic properties of dual phase cobalt ferrite, Scient. Rep. 7 (2017) 2524, https://doi.org/10.1038/s41598-017-02784-z.
[14] K.K. Bharathi, R.J. Tackett, C.E. Botez, C.V. Ramana, Co existence of spin glass behavior and long-range ferromagnetic ordering in La and Dy- doped Co ferrite, J. Appl. Phys. 109 (2011), https://doi.org/10.1063/1.3562201.
[15] M.A. Almessiere, Y. Slimani, I.A. Auwal, S.E. Shirsath, A. Manikandan, A. Baykal, B. Özçelik, I. Ercan, S.V. Trukhanov, D.A. Vinnik, A.V. Trukhanov, Impact of Tm^{3+} and Tb^{3+} rare earth cations substitution on the structure and magnetic parameters of Co-Ni nanospinel ferrite, Nanomaterials 10 (2020) 2384, https://doi.org/10.3390/nano10122384.
[16] E. Pervaiz, I.H. Gul, Influence of rare earth (Gd^{3+}) on structural, gigahertz dielectric and magnetic studies of cobalt ferrite, J. Phys. Conf. 439 (2013), 012015, https://doi.org/10.1088/1742-6596/439/1/012015.

[17] M.A. Almessiere, Y. Slimani, A. DemirKorkmaz, A. Baykal, H. Gungunes, H. Sozeri, Sagar E. Shirsath, S. Guner, S. Akhtar a, A. Manikandan, Impact of La^{3+} and Y^{3+} ion substitutions on structural, magnetic and microwave properties of $Ni_{0.3}Cu_{0.3}Zn_{0.4}Fe_2O_4$nanospinel ferrites synthesized via sonochemical route, RSC Adv. 9 (2019) 30671–30684, https://doi.org/10.1039/c9ra06353f.

[18] M. Hashim, A. Ahmed, S. Asad Ali, S.E. Shirsath, M.M. Ismail, R. Kumar, S. Kumar, S.S. Meena, D. Ravinder, Structural, optical, elastic and magnetic properties of Ce and Dy doped cobalt ferrites, J. Alloys Compd. 834 (2020), 155089, https://doi.org/10.1016/j.jallcom.2020.155089.

[19] R. Indhrajothi, I. Prakash, M. Venkateswarlu, N. Satyananayana, Lanthanum ion (La^{3+}) substituted $CoFe_2O_4$ anode material for Lithium ion battery applications, New J. Chem. 39 (2015) 4601–4610, https://doi.org/10.1039/C5NJ00791G.

[20] P. Kumar, S.K. Sharma, M. Knobel, M. Singh, Effect of La $^{3+}$ doping on the electric, dielectric and magnetic properties of cobalt ferrite processed by co-precipitation technique, J. Alloys Compd. 508 (2010) 115–118, https://doi.org/10.1016/j.jallcom.2010.08.007.

[21] S.B. Das, R.K. Singh, V. Kumar, N. Kumar, P. Singh, N.K. Naik, structural, magnetic, optical and ferroelectric properties of Y^{+3} substituted cobalt ferrite nanoparticles prepared by a cost effective sol-gel rout, Mater. Sci. Semicond. Process. 145 (2022), 106632, https://doi.org/10.1016/j.mssp.2022.106632.

[22] B.I. Salem, O.M. Hemeda, S.F. Mansour, Morphological, infrared and structural studies for nano cobalt ferrite doped with lanthanum, Delta J. Sci. 38 (2017) 94–114.

[23] S. Dabagh, K. Chaudhary, Z. Haider, J. Ali, Study of structural phase transformation and hysteresis behavior of inverse-spinel-ferrite nanoparticles synthesized by co-precipitation method, Results Phys. 8 (2018) 93–98, https://doi.org/10.1016/j.rinp.2017.11.033.

[24] G.K. Williamson, W.H. Hall, Discussion of the theories of line broadening, Acta Metall. 1 (1953) 22–31, https://doi.org/10.1016/0001-6160(53)90006-6.

[25] M.H.A. Begum, N. Khatun, S. Islam, N.A. Ahmed, M.S. Hossain, M.A. Gafur, A. Siddika, Synthesis and characterization of structural, magnetic and electrical properties of Ni–Mn–Zn ferrites, Int. J. Nanoelectr. Mater. 11 (2018) 15–24.

[26] R.S. Yadav, I. Kuritka, J. Vilcakova, J. Havlica, L. Kalina, P. Urbanek, M. Machovsky, M. Masar, M. Holek, Influence of La^{+3} on structural, magnetic, dielectric, electrical and modulas spectroscopic characteristics of single phase $CoLa_xFe_{2-x}O_4$ nanoparticles, J. Mater. Sci. Mater. Electron. 28 (2017) 9139–9154, https://doi.org/10.1007/s10854-017-6648-5.

[27] S.R. Sawant, S.S. Suryavanshi, Iono-covalent and Yafet Kittle (YK) angle studies of slow cooled and quenched CuZn-system, Curr. Sci. 57 (1998). https://www.jstor.org/stable/24091570.

[28] S.B. Das, R.K. Singh, V. Kumar, N. Kumar, P. Singh, N. Kumar Naik, Structural, magnetic, optical and ferroelectric properties of Y^{3+} substituted cobalt ferrite nanomaterials prepared by a cost-effective sol-gel route, Mater. Sci. Semicond. Process. 145 (2022), 106632, https://doi.org/10.1016/j.mssp.2022.106632.

[29] S.S. Satpute, S.R. Wadgane, K. Desai, D.R. Msne, R.H. Kadam, Substitution effect of Y^{+3} ions on the structural, magnetic and electrical properties of cobalt ferrite nanoparticles, Cerâmica 66 (2020) 43–49, https://doi.org/10.1590/0366-69132020663772734.

[30] S. Zara, A.A. Ati, S. Dabagh, R.M. Rosemao, Z. Othaman, Synthesis structure and magnetic behavior studies of Zn–Al substituted cobalt ferrite nanoparticles, J. Mol. Struct. 1089 (2015) 25–31, https://doi.org/10.1016/j.molstruc.2015.02.006.

[31] K.A. Ganure, V.T. Katkar, L.A. Dhale, K.S. Lohar, Infrared spectral and elastic moduli study of Pr^{+3} doped Ni-Co-Zn ferrite via normal micelles method, Int. J. Chem. Eng. Res. 9 (2017) 153–161. http://www.ripublication.com.

[32] K.A. Mohammed, A.D. Al-Rawas, A.M. Gismelseed, A. Sellai, H.M. Widatallah, A. Yousif, M.E. Elzain, M. Shongwe, Infrared and structural studies of $Mg_{1-x}Zn_xFe_2O_4$ferrites, Phys. B Condens. Matter 407 (2012) 795–804, https://doi.org/10.1016/j.physb.2011.12.097.

[33] P.P. Hankare, K.R. Sanadi, K.M. Garadkar, D.R. Patil, I.S. Mulla, Synthesis and characterization of nickel substituted cobalt ferrite nanoparticles by sol-gel auto combustion method, J. Alloys Compd. 553 (2013) 383–388, https://doi.org/10.1016/j.jallcom.2012.11.181.

[34] P.S. Aghav, V.N. Dhage, M.L. Mane, D.R. Shengule, R.G. Dorik, K.M. Jadhav, Effect of Aluminum substitution on the structural and magnetic properties of cobalt ferrite synthesized by sol-gel auto combustion process, Phys. B Condens. Matter 406 (2011) 4350–4354, https://doi.org/10.1016/j.physb.2011.08.066.

[35] S. Sing, B.C. Yadav, V.D. Gupta, P.K. Dwivedi, Investigation on effects of surface morphologies on response of LPG sensor based on nanostructured copper ferrite system, Mater. Res. Bull. 47 (2012) 3538–3547, https://doi.org/10.1016/j.materresbull.2012.06.064.

[36] R.S. Yadva, I. Kuritka, J. Vilcakova, J. Havlica, J. Masilko, L. Kalina, J. Tkacz, J. Svec, V. Enev, M. Hajduchov, Impact of grain size and structural changes on magnetic, dielectric, electrical, impedance and modulas spectroscopic charecteristics of $CoFe_2O_4$nano particles synthesized by honey mediated sol-gel combustion method, Adv. Nat. Sci. Nanosci. Nanotechnol. 8 (2017), 045002, https://doi.org/10.1088/2043-6254/aa853a.

[37] S.I. Amad, D. Ravi Kuumar, I.A. Syed, R. Satar, S.A. Ansari, Strructural, Spectroscopic and magnetic study of nano crystalline cerium-substituted Magnesium ferrites, Arabian J. Sci. Eng. (2017) 389–398, https://doi.org/10.1007/s13369-016-2297-x.

[38] L.B. Tahar, M. Artus, S. Ammar, L.S. Smiri, F. Herbest, M.J. Vaulay, V. Richard, J.M. Greneche, F. Villain, F. Fievet, Magnetic properties of $CoFe_{1.9}RE_{0.1}O_4$ nanoparticles (RE=La,Ce, Nd, Sm, Eu, Gd, Tb, Ho) prepared in polyol, J. Magn. Magn Mater. 320 (2008) 3242–3250, https://doi.org/10.1016/j.jmmm.2008.06.031.

[39] M.A. Iqbal, M. Islam, M.N. Ashiq, I. Ali, A. Iftikar, Effect of Ga- substitution on physical and magnetic properties of $Li_{1.2}Mg_{0.4}Gd_xFe_{2-x}O_4$ferite, J. Alloys Compd. 579 (2013) 181–186, https://doi.org/10.1016/j.jallcom.2013.06.033.

[40] F.X. Chen, J.T. Jia, Z.G. Xu, B. Zhou, C.S. Liao, C.H. Yan, L.Y. Chen, H.B. Zhao, Microstructure, magnetic, and magneto-optical properties of chemical synthesized Co-RE (RE = Ho, Er, Tm, Yb, Lu) ferrite nanocrystalline films, J. Appl. Phys. 86 (1999) 2727, https://doi.org/10.1063/1.371117.

[41] A. Chandran, K.C. George, Defect induced modifications in the optical, dielectric and transport properties of hydrothermally prepared Zn Snanoperticles and nanorods, J. Nanoparticle Res. 16 (2014) 2238, https://doi.org/10.1007/s11051-013-2238-5.

[42] M. Naeem, N.A. Shah, I.H. Gul, A. Maqsood, Structural, electrical and magnetic characterization of Ni-Mg spinel ferrites, J. Alloys Compd. 487 (2009) 739–743, https://doi.org/10.1016/j.jallcom.2009.08.057.

[43] C.G. Koops, On the dispersion of resistivity and dielectric constant of some semiconductors at audio frequencies, Phys. Rev. 83 (1951) 121–124, https://doi.org/10.1103/PhysRev.83.121.

[44] S.A. Saafan, S.T. assar, Dielectric behavior of nano-structured and bulk LiNiZn ferrites samples, J. Magn. Magn Mater. 324 (2012) 2989–3001, https://doi.org/10.1016/j.jmmm.2012.04.037.

[45] M.A. Rahman, A.K.M.A. Hossain, Electrical transport properties of Mn–Ni–Zn ferrite using complex impedance spectroscopy, Phys. Scripta 89 (2014), 025803, https://doi.org/10.1088/0031-8949/89/02/025803.

[46] R.V. Mangalaraja, S. Ananthakumar, P. Manohar, F.D. Gnanam, Magnetic, electrical and dielectric behaviour of $Ni_{0.8}Zn_{0.2}Fe_2O_4$ prepared through fash combustion technique, J. Magn. Magn Mater. 253 (2002) 56–64, https://doi.org/10.1016/S0304-8853(02)00413-4.

[47] C. Murugesan, G. Chandrasekaran, Impact of Gd^{3+}substitution on the structural, magnetic and electrical properties of cobalt ferrite nanoparticles, RSC Adv. 5 (2015) 73714–73725, https://doi.org/10.1039/C5RA14351A.

[48] D.M. Jnaneshwara, D.N. Avadhani, B. Daruka Prasad, H. Nagabhushana, B.M. Nagabhushana, S.C. Sharma, S.C. Prashantha, C. Shivakumar, Role of Cu^{2+} ions substitution in magnetic and conductivity behaviour of nano $CoFe_2O_4$, Spectrochim. Acta Part A Molecular and Biomolecular Spectroscopy 132C (2014) 256–262, https://doi.org/10.1016/j.saa.2014.04.179.

[49] S. Islam, N. Khatun, M.S. Habib, S.F.U. Farhad, N.I. Tanvir, M.A.A. Shaikh, S. Tabassum, D. Islam, M.S. Hossain, A. Siddika, Effects of yttrium doping on structural, electrical and optical properties of barium titanate ceramics, Heliyon 8 (2022), e10529, https://doi.org/10.1016/j.heliyon.2022.e10529.

[50] J. Tauc, R. Grigorovici, A. Vancu, Optical properties and electronic structure of amorphous germanium, Phys. Status Solidi 15 (1996) 627–637, https://doi.org/10.1002/pssb.19660150224.

[51] R.B. Kale, C.D. Lokhande, Influence of air annealing on thestructural, optical and electrical properties of chemically deposited Cd Senano-crystallites, Appl. Surf. Sci. 223 (2004) 343–351, https://doi.org/10.1016/j.apsusc.2003.09.022.